PCCP

Accepted Manuscript

ROYAL SOCIETY OF CHEMISTRY

www.rsc.org/pccp

Defects-Assisted Ferromagnetism due to Bound Magnetic Polaron in Ce into Fe, Co:ZnO nanoparticles and First-Principle Calculations

*Kuldeep Chand Verma[1] and R.K. Kotnala[2]

[1]*Centre of Advanced Study in Physics, Department of Physics, Panjab University, Chandigarh 160 014, India*
[2]*CSIR-National Physical Laboratory, New Delhi 110012, India*

Abstract

The $Zn_{0.94}TM_{0.03}Ce_{0.03}O$ [$Zn_{0.94}Fe_{0.03}Ce_{0.03}O$ (ZFCeO) and $Zn_{0.94}Co_{0.03}Ce_{0.03}O$ (ZCCeO)] nanoparticles were synthesized by sol-gel process. The elemental analysis detects the weight percentage of Zn, Co, Fe, Ce and O in each sample. The Rietveld refinement of X-ray diffraction pattern gives the occupancy of dopant atoms, Wurtzite ZnO structure, crystallinity and lattice deformation with doping. The Ce doping into ZFO and ZCO form nanoparticles than nanorods that described due to chemical and ionic behavior of Ce, Fe, Co and Zn ions. The Raman active modes have peak broadening, intensity and shifting with doping to induce lattice defects. PL spectra show blueshift at near-band-edge and defects influences broad visible emission with Ce doping. An enhancement in ferromagnetism in the magnetic hysteresis at 5 K is measured. The zero-field cooling and field cooling at H=500 Oe at temperature, T = 300 - 5 K could confirm antiferromagnetic interactions which mediated by defect carriers. The bound magnetic polaron at defect sites are responsible in observed ferromagnetism. The ac magnetic susceptibility measurements determine the antiferromagnetic to ferromagnetic transition with some magnetic clustered growth in the samples and reveal a frequency independent peak to show Neel temperature. Weak room temperature ferromagnetism and optical quenching in ZFCeO is described by valance states of Fe and Ce ions, respectively. Using first-principle calculations we have studied the occupancy of Ce replaced Zn atom in the Wurtzite structure.

* Corresponding authors. Tel: +91-9418941286

E-mail: kuldeep0309@yahoo.co.in ; dkuldeep.physics@gmail.com

Keywords: A. Nanoparticles B. TEM C. defects/vacancies D. 4*f*-5*d*-3*d* transition E. antiferromagnetism

1. Introduction

Diluted magnetic semiconductor (DMS) ZnO is a wide band gap that has gained recent research in spintronics, due to the ability to change its optical and magnetic behavior with doping of transition metals, TM (=Fe, Co, Mn, Ni, Cu, Cr, or V) ions [1-4]. DMS ZnO with Co and Fe doping is widely studied for room temperature ferromagnetism (RTFM). Walsh *et al.* [5] suggest carrier mediated magnetism for Co:ZnO with weak antiferromagnetic (AFM) ordering through Co t_{2d} states. However, Fe:ZnO involve double exchange mechanism Fe^{2+}-Fe^{3+} via oxygen vacancies that proposed by Zener [6]. It has O-2p orbitals that could show a spin polarization induced by Fe doping [7]. Recently, it has been suggested that the presence of multivalent ions in the ZnO lattice achieved ferromagnetism with Curie temperature above room temperature [8,9]. In fact, the simultaneous doping from TM and rare earth (RE) ions into ZnO has two kinds of defects, especially multi-valence ions [10], could tailor the position and occupancy of the Fermi energy to modify the magnetic behavior [11].

Recently, the RE Ce ions based DMS ZnO has been hardly studied [11-13]. Babu *et al.* [11] give redox Ce^{3+}/Ce^{4+} formation during oxidizing and reducing conditions due to incorporation of Ce into TM oxides. It suggested that the Ce doping into ZnO may induce defects/oxygen vacancies for magnetic exchange interactions. The 4*f* electrons in Ce are tightly bound around the nucleus and shielded by $5s^2p^6d^16s^2$ electrons, leading to strong local spin. It is difficult for Ce doped TM:ZnO to have the 4*f*-4*f* and 4*f*-3*d* exchange interaction without a medium. The localized *f* electrons make the nomadic *s* electrons spin polarization a medium, leading to a 4*f*-4*f* exchange interaction, which is a cruise electron transfer exchange interaction in two local spins without interaction. This is described by RKKY model [13].

Yao *et al.* [14] suggested AFM interactions in Ce-Ce due to short distances between them. For Ce doped TM:ZnO, the larger ratio of dopant cation to cation radius structure causes more defects, leading to a larger concentration of electrons and holes. The ionic size of dopant influences the bond angle, thereby changing the matrix element that could describe electron hopping and electronic charge concentration, resulting into changing magnetic transition [15]. Therefore, the magnetic phase transition for TM:ZnO DMS system may influence by Ce ions due to larger ionic size of Ce than TM ions. The defects carriers act as a medium of magnetic interactions that given by Coey *et al.* [16]. It suggested that the ferromagnetism in intrinsically n-type semiconductors and insulators involves a model where shallow donor electrons, created due to intrinsic defects in the semiconductors, form bound magnetic polarons (BMPs) with magnetic cations.

In the present paper, the $Zn_{0.94}TM_{0.03}Ce_{0.03}O$ [$Zn_{0.94}Fe_{0.03}Ce_{0.03}O$ (ZFCeO) and $Zn_{0.94}Co_{0.03}Ce_{0.03}O$ (ZCCeO)] nanoparticles have been synthesized by sol-gel method. The structural, microstructural, Raman modes, luminescent, magnetic properties and first-principle calculation have been investigated in this paper.

2. Experimental details

2.1. Synthesis of Ce (=3 mol%) doped $Zn_{0.97}Fe_{0.03}O$ (ZFO) and $Zn_{0.97}Co_{0.03}O$ (ZCO) nanoparticles

For the synthesis of ZFCeO and ZCCeO nanoparticles, a sol-gel based chemical process using polyvinyl alcohol (PVA) as surfactant was used. The precursor solutions were prepared from zinc acetate, ferric chloride, cobalt chloride and cerium chloride with a desired molar concentration in each sample. In this method, ethanol and acetic acid were mixed in 3:1 ratio. Zinc acetate was added to it and stirred for 2 h on magnetic stirrer. This solution was prepared separately for both ZFCeO and ZCCeO samples. The dopants (Fe, Co and Ce) were added in each sample in the desired stoichiometric ratio and again stirred for 1 h. The

precursor solution (M) in each sample was mixed in PVA solution, *i.e.*, M: PVA::5:2. The solution was dried at 250 ^{o}C and annealed at 700 ^{o}C for 2 h for crystallization.

2.2. Characterization

Elemental analyses of the samples were performed through X-ray fluorescence (XRF) spectroscopy using Cu K_{α} radiation on WD-XRF (Model: S8 TIGER; Make: Bruker, Germany). The crystalline structure was analyzed by the X-ray diffraction (XRD) by using X'Pert PRO PANalytical system. Transmission Electron Microscopy (TEM) was used to analyse the microstructural properties (HITACHI H-7500). The Raman spectrum and photoluminescence (PL) of the samples were recorded on Renishaw UK consists of Ar ion laser with 518 nm wavelength and 50 mW power. Magnetization of the samples was studied with a superconducting quantum interference device (SQUID) magnetometer (Quantum Design, Inc. U.S.A.) for the temperature, T = 5 - 300 K range and magnetic fields, H = -5 to +5 kOe. The temperature dependent magnetization [M(T)] measurements were carried out at zero field cooled (ZFC) and field cooled (FC) conditions at H=500 Oe. The real, $\chi'(T)$, and imaginary, $\chi''(T)$, components of the complex ac susceptibility, $\chi(T)$, measurements were done with the Quantum Design magnetometer using an oscillating field H_{ac} = 2.5 Oe for frequencies of 100, 300, 500 and 1000 Hz at T = 10 – 100 K, without any dc field bias. Samples were measured from a demagnetized state, cooling in zero field with no dc field applied to maximize the ac signals. It is to be noted that a small enough ac magnetic field, H_{ac}, enables us to measure the true spin susceptibility of a magnetic system. The limit of this field is again determined by the sensitivity of the set up itself. The magnetic data were corrected for diamagnetic contributions of the sample holder. X-ray photoelectron spectroscopy (XPS) was performed using a Perkin-Elmer model 1257 equipped with a non-monochromatized Al K_{α} X-ray source.

2.3 Detail of Computational method

In the survey to TM substituted DMS ZnO, it has been found that the TM ions occupies Zn atomic site in the Wurtzite structure [17]. Chang *et al.* [18] revealed that Co dopant most likely substitute for Zn atoms and that free charge carriers are absent for a wide range of Co concentrations. Due to this, the interstitial Co impurities and charged oxygen vacancies are energetically less favorable than substitutional Co atoms. Density functional theory (DFT) predicts occupancy of Fe ions into Zn and AFM ordering in ZnO [19]. The first principle calculation by Aravindh *et al.* [20] found that an isolated Gd atom incorporated in a Zn site exhibit a magnetic moment ~6.87μ_B, for all Gd positions. Bantounas *et al.* [21] also give the occupancy of RE ions into Wurtzite ZnO structure using DFT calculation within generalized gradient approximation (GGA). They suggest V_{Zn}-Gd complex which is highly favorable. In the light of above discussion, we have understood that both the TM and RE ions are replaced by Zn atoms in the Wurtzite structure. Therefore, it is important to study their occupancy when TM and RE ions are simultaneously doped into ZnO. In the present DMS systems, TM=Fe, Co and RE=Ce ions. For this, we have applied the first principle DFT calculation. We have replaced nearest/non-nearest neighbor Zn atom to TM=Fe, Co by Ce ions and calculate the stability of Ce atoms within Wurtzite structure.

The first-principle calculation using DFT have been carried using *ab initio* calculations which were performed using a projector augmented-wave (PAW) method within the GGA adopting the Perdew-Burke-Ernzerhof (PBE) exchange correlation potentials implemented in ABINIT [22, 23]. The DFT has performed on ZFCeO and ZCCeO samples within ZnO supercell consisting of 72 atoms. The GGA has been corrected by Hubbard-U terms. Here we use typical values of U = 4.5 eV on Zn, Fe, Co [19] and 5.0 eV for Ce [24]. The plane wave cutoff energy used is 20 Hartree (1 Ha=27.2113845 eV). The forces acting on the atoms are less than 0.0025 eV/Å in relaxed structure. Brillouin zone integrations were performed by 3×3×3 Monkhorst and Pack special point grids [25]. The Ce atom is placed on

Zn sites that nearest neighbor [Fig.9(a) & (c)] and non-nearest neighbor [Fig.9(b) & (d)] to the TM:Fe,Co atoms in the ZnO Wurtzite supercell, respectively. The binding energy equivalent to each relaxed Wurtzite ZnO structure corresponds to ZFCeO and ZCCeO is calculated. The binding energy difference (ΔE) is here the difference among nearest neighbor and non-nearest neighbor Ce substituted Zn atom to the TM:Fe,Co, respectively.

3. Result and discussion

A typical XRF pattern of Ce doped ZFO and ZCO is shown in Fig. 1. The pattern shows the presence of Zn, Fe, Ce and O of ZFCeO and Zn, Co, Ce and O of ZCCeO with nominal concentration of each equal to the initial precursor composition, respectively. The elemental concentration in weight percentage is given in Fig.1. The weight percentage error is around 0-1%.

Figure 2 shows the XRD results for Ce doped ZFO and ZCO nanoparticles using the refined Rietveld pattern (FULLPROF Program). All refinements were performed using the space group $P6_3mc$. The Rietveld refinement initiated with Zn^{2+} and O^{2-} atoms located at (1/3, 2/3, 0) and (1/3, 2/3, z), respectively. The fitted curves match quite well with the experimental data. In the refinement process, the Co, Fe and Ce occupancy were varied for the two Zn and O sites to locate their exact site. The best fit was obtained when Co, Fe and Ce atoms occupy the Zn site with total preference while the dopant occupy on the O site gave very poor fits. The XRD reflections results into hexagonal Wurtzite ZnO phase. The diffraction peaks are observed at 2θ = 31.81, 34.54, 36.36, 47.72 and 56.81^o corresponding to (100), (002), (101), (102) and (110), respectively. No impurity peaks of oxide phases are observed. The minor splitting of (102) and (110) peak might be due to the slight cubic zinc blende (220) and (311) phase formation, respectively [26]. The refined lattice parameters are a(Å) = 3.259(1) and 3.262 (3), c(Å) = 5.215 (3) and 5.218 (2), unit cell volume (V) = 47.9682 (3) Å^3 and 48.0828 (2) Å^3, bond length (l_{Zn-O}) = 1.9826 Å and 1.9842 Å, R_p(%) = 6.57 and

6.95, R_{wp} (%) = 9.0 and 9.8, and χ^2 = 1.97 and 2.05, respectively, for ZFCeO and ZCCeO sample.

The lattice parameters for hexagonal Wurtzite ZnO structure are also calculated using [27]:

$$\frac{1}{d^2} = \frac{4}{3}\frac{(h^2+hk+k^2)}{a^2} + \frac{l^2}{c^2} \quad (1)$$

where *a* and *c* are the lattice constants; *h*, *k* and *l* are the Miller indices; and *d* is the interplanar spacing. The calculated values of the lattice parameters for pure [27] and Ce doped ZFO and ZCO are given in table 1. The value of distortion ratio is 1.5987, 1.5988, 1.5994 and 1.5998, respectively, calculated for ZFO, ZCO, ZFCeO and ZCCeO. The calculated values of *c*/*a* ratio of ZFO and ZCO are slightly increased than pure ZnO (*c*/*a*~1.598) [3] due to shape/size effect of nanorods [27]. But it is again enhanced with RE:Ce ions due to ionic size effect.

The bond length, $l_{Zn\text{-}O}$ of Ce doped ZFO and ZCO has been calculated using [28]:

$$l_{Zn-O} = \sqrt{\frac{a^2}{3} + \left(\frac{1}{2} - u\right)^2 c^2} \quad (2)$$

where *a* and *c* are lattice constants.

$$u = \frac{a^2}{3c^2} + 0.25 \quad (3)$$

where *u* is a positional parameter.

The values of $l_{Zn\text{-}O}$ are given in table 1 which show an enhancement with Ce doping. The volume per unit cell for the hexagonal system has been calculated using [28]

$$V = 0.866 \times a^2 \times c \quad (4)$$

The value of unit cell volume is given in table 1 for pure and Ce doped ZFO and ZCO. The values of lattice parameters given in table 1 are consistent with those refined by Rietveld method. Therefore, the observed variation in lattice parameters with doping must be induced

displacement of atoms in the Wurtzite ZnO structure. It results into defects such as vacancies or interstitials in the lattice.

Figure 3 shows the TEM images of Ce doped ZFO and ZCO nanoparticles at different magnification applied in each sample. The pure samples of ZFO [*D* (diameter) =14 nm and *L* (length)=50 nm] and ZCO [*D*=63 nm and *L*=131 nm] are nanorods [27]. It means the dopant Ce ions results to deform shape of ZnO nanorods into nanoparticles. The average size, *D*, of nanoparticles is 97±4 nm and 106±3 nm, respectively, measured for ZFCeO and ZCCeO. The variation in the value of *D* is explained on the basis of ionic radii differences between Zn and dopant ions, *i.e.* Zn^{2+} (0.60 Å), Fe^{3+} (0.49 Å), Co^{2+} (0.58 Å) and Ce^{3+} (1.01 Å). The inset in the TEM images [Fig.3 (right)] is the high-resolution TEM (HRTEM) images to show the crystalline formation and lattice spacing after doping into ZnO lattice. It shows that the distorted lattice has an enhanced interplanar spacing *d* [corresponding to (101) planes] ~ 0.247 and 0.250 nm, respectively, measured for ZFCeO and ZCCeO. For pure ZnO, the value of *d* ~0.237 nm reported in the JCPDS data. In the HRTEM images, some little spots that covered lattice fringes of spacing are also observed. This is an indication of the ferromagnetic clusters or structural inclusions which may found within the lattice or on the surface of nanoparticles. The high crystallinity of the nanoparticles is also evident from the selected area electron diffraction (SAED) patterns [insets of the Fig.3(left)], respectively. The formation of diffraction rings in SAED pattern indicates the polycrystalline phase of ZnO.

The mechanism in the formation of nanoparticles of Ce doped ZFO and ZCO is described due to agglomeration of Zn^{2+} and OH^- ions of high energy surfaces [29]. Due to low stability of Zn^{2+}, Fe^{3+} and Co^{2+} ions with PVA [27], the oriented attachment is easily formed. But in the present samples, the nanostructural agglomeration is formed due to larger ionic radii and octahedral environment of Ce ions. In addition, the nanoparticles are also formed due to the simulations of ZnO aggregation $[Zn_x(OH)_y]^{(2x-y)+}$ which change in both size

and configuration through proton transfer [30]. In the present study, the chemical behavior of Zn^{2+} ions involves:

$$Zn(CH_3COO)_2 \leftrightarrow Zn^{2+} + 2CH_3COO^- \quad (5)$$

$$2H_2O + 2e^- \rightarrow H_2 + 2OH^- \quad (6)$$

$$Zn^{2+} + 2OH^- \rightarrow Zn(OH)_2 \quad (7)$$

$$Zn(OH)_2 + 2OH^- \leftrightarrow [Zn(OH)_4]^{2-} \rightarrow ZnO + H_2O + 2OH^- \quad (8)$$

The aggregation surface mainly consists Zn^{2+} and OH^-ions, the core comprises Zn^{2+} and O^{2-} ions, only [30]. The dissociation of water and Zn^{2+}/OH^- ions from the aggregates stabilized into: (i) ripening reactions leading to the formation of O^{2-}ions and (ii) nucleation and growth of a ZnO domain of Wurtzite structure. It is well-known that ZnO is a polar crystal, having positively Zn^{2+}-terminated (0001) and negatively O^{2-}-terminated (000-1) polar surfaces, which induced a net dipole moment along the *c* axis [31]. The surface energies of the polar {0001}plane are higher than nonpolar {01-10} and {2-1-10}. So, the preferential growth along the *c*-axis is energetically favorable. Thus, the pure sample of ZnO has nanorods [27]. However, the dopants Co and Fe involves following [32, 33]:

$$Fe^{3+} + e^- \leftrightarrow Fe^{2+} \quad (9)$$

$$Fe^{2+} + 2H_2O \leftrightarrow Fe(OH)_2 + 2H^+ \quad (10)$$

$$Fe^{3+} + 3H_2O \leftrightarrow Fe(OH)_3 + 3H^+ \quad (11)$$

$$Fe(OH)_2 + OH^- \leftrightarrow FeOOH + H_2O + e^- \quad (12)$$

$$2Fe(OH)_3 + Fe(OH)_2 \rightarrow Fe_3O_4 + 4H_2O \quad (13)$$

$$Co^{2+} + 2OH^- \rightarrow Co(OH)_2 \quad (14)$$

$$Co(OH)_2 + OH^- \leftrightarrow CoOOH + H_2O + e^- \quad (15)$$

$$CoOOH + OH^- \leftrightarrow CoO_2 + H_2O + e^- \quad (16)$$

The reaction mechanism (9)-(13) is given by Zhang *et al.* [32] using hard-soft acid-base theory for crystallization of FeOOH with different morphologies. The $Fe(OH)_2$ and

$Fe(OH)_3$ products are easily formed nanorods [27]. However, Xia *et al.* [33] suggested aggregation among Co^{2+} and OH^- ions that involve equations (14)-(16). Due to this, the dimensional ratio of the ZFO nanorods is enhanced than ZCO [27].

The incorporation of Ce ions involves large ionic aggregation type product with ZFO and ZCO due to comparatively higher ionic environment of Ce than Fe,Co. It forms Ce/OH^-complexes [34]:

$$Ce^{3+} + OH^- + \frac{1}{2}H_2O_2 \rightarrow Ce(OH)_2^{3+} \quad (17)$$

$$Ce(OH)_2^{3+} + 2OH^- \rightarrow Ce(OH)_4 \rightarrow CeO_2 + 2H_2O \quad (18)$$

It is well known that Ce can exist into two 3+ and 4+ oxidation states via oxygen vacancies and, therefore, the resulting aggregation of ZFCeO and ZCCeO is energetically favoured [34]. The Ce atom has the ability to easily and drastically adjust its electronic configuration due to oxygen vacancies, or defects, in the lattice structure that arise through loss of oxygen and/or its electrons during redox reactions [35]. The Ce^{4+} and the low formation energies of surface vacancies are important for oxidation, whereas the Ce^{3+} and electron shuffling within the lattice oxygen vacancies provide power for reduction. Thus, the final product with Ce doped ZFO and ZCO samples is nanoparticles that nanorods.

Figures 4 shows Raman scattering of pure and Ce doped ZFO and ZCO nanoparticles. It exhibits vibrational modes peaked around 191, 312, 419, and 518 cm^{-1}, which correspond to processes [2TA; $2E_2$(low)], E_2(high)-E_2(low), E_2(high) and [$2B_1$ low; 2LA], respectively. The presence of high intensity E_2 mode and negligible E_1(LO) mode indicate that the increased Raman scattering due to good crystalline quality [36]. This is consistent with XRD results. The variation in Raman bands exists due to nano size effect [36]. Since the nonpolar E_2(high) phonon mode is generally observed at 437 cm^{-1}. In the present samples, this E_2(high) mode is frequency shifted with doping. For Ce doped ZFO and ZCO samples, the E_2(high) mode shifted towards higher frequency due to the compressive stress in nano grains. Ahmed

et al. [31] suggested E_2(high) mode shifting due to an increased binding energy of Zn-O bonds. We have also observed a broad band at ~500–600 cm^{-1} which appears to enclose multi peaks. Instead [$2B_1$ low; 2LA], the main peak is centred at ~556 cm^{-1} which is not attributed to ZnO mode and can be indexed to an additional mode (AM). Also, the [$2B_1$(low); 2LA] is the disorder-activated mode due to the relaxation of Raman selection rules that is induced by the breakdown of the crystal symmetry [37]. Kumar *et al.* [28] observed phonon mode at 547 cm^{-1} which is similar to AM shown in Fig.4. It exist due to the shallow donor defects, such as zinc interstitials (Zn_i) and/or oxygen vacancies, bound on the tetrahedral Co-sites. The LA/LO+TO modes at 836 and 1030 cm^{-1} exist due to fingerprint vibration of the O-O peroxide group which suggested by Herring *et al.* [38]. The 2LO mode at 1119 cm^{-1} has higher phonon density states, and induced by impurities and intrinsic defects. The vibrational modes [2TA; $2E_2$(low)] and E_2(high)-E_2(low) are an indication to oxygen defects or vacancies in ZnO lattice [39].

Figures 5 shows PL spectra of pure and Ce doped ZFO and ZCO nanoparticles. The emission peaks for ZFCeO (404 nm) and ZCCeO (379 nm) are existed due to near-band-edge (NBE) emission [40]. When we compared the results of NBE [Fig. 5] with pure ZFO (393 nm), ZCO (394 nm) and ZnO (413 nm) [27], the Ce doped samples observed peak shifting. It has blueshifting behavior involve Moss-Burstein band filling effect given by Tong *et al.* [41]. This is due to an increase in the carrier concentration with TM and Ce ions in ZnO will cause Fermi level to move into the conduction band. However, the low wavelength region, 325-365 nm [Fig.5(b)] show characteristic PL emission bands centred at 328, 331, 337, 344, 351, 358 and 363 nm which is equivalent to the band gap 3.78, 3.75, 3.68, 3.60, 3.53, 3.46 and 3.42 eV, respectively, for Co doped samples. These optical transitions attribute to the band gap transition $O^{2-} \rightarrow Co^{2+}$ with charge transfer process from the valence band of the Co_3O_4 [11]. It comprised a mixture $Co^{2+,3+}$ 3*d* and O 2*p* states. It may also contribute from surface exciton

recombination by nanoparticles have higher specific surface area [42].

As shown in Fig.5, the higher wavelength region is the visible which is generally believed to be generated by deep level defects. In pure ZFO and ZCO samples, the negligible emission is found in the visible region than NBE. But the Ce doped ZFO and ZCO samples show a broad visible emission that may comprised from multiple peaks. Mainly, the higher intense peaks lie in green-orange (523, 525, 528, 545, 546, 572 and 583 nm) region. When we considered Ce-ions, there are two different oxidation states (Ce^{4+} and Ce^{3+}) which play a key role in changing the optical behavior. It is well known that the Ce^{4+} ions have a powerful tendency to attract electron, while the Ce^{3+} ions suffer from oxidation, easily [43]:

$$2CeO_2 + H_2O \rightarrow Ce_{1-x}^{4+}Ce_x^{3+}O_{2-x/2} + 2H^+ + 2e^- + (6+x)/4\ O_2 \qquad (19)$$

The formation of Ce^{3+} from (19) have the possibility of transition between 5*d* and 4*f* orbitals, which led to the quenching of the blue and green emission [Fig.5]. But ZCCeO depicts comparatively smaller magnitude in visible emission intensity. It may due to the formation of Ce^{4+} ions in majority than Ce^{3+} cause lower luminescent centers [11]. Moreover, green band emission can be attributed to the singly ionized oxygen vacancy which resulted from the recombination of photogenerated hole with single ionized charge state defect [44]. For RE ions doped semiconductor, the transfer of energy from the host to RE ions often can result into strong suppression and/or modification of the host luminescence [45]. Thus, the incorporation of Ce into ZnO lattice takes enough energy from Fe,Co ions to affect the band gap structure due to the production of multi-emission centres. It must form Zn, Co and Fe interstitials and oxygen vacancy. In addition, the strongest green band intensity must correspond to the higher surface-to-volume ratio of nanoparticles which involve large amount of surface oxygen vacancies [42].

Figures 6(c' & d') shows the ferromagnetic behavior of Ce doped ZFO and ZCO nanoparticles by measuring magnetization (*M*) versus magnetizing field (*H*) hysteresis at 5 K.

Both samples show paramagnetism [Fig. 6(b)] at room temperature (=300 K) measurement but the slight ferromagnetic interactions observed only in ZFCeO. At 5 K measurement, the values of saturation magnetization (M_s) are 0.339 and 0.478 emu/g, and remanent magnetization (M_r) are 0.135 and 0.162 emu/g with coercivity (H_c) 753 and 197 Oe, respectively, measured for ZFCeO and ZCCeO. We observed enhancement in both M_r and H_c values than for pure ZFO (M_s~ 0.459 emu/g, M_r~0.059 emu/g and H_c~35 Oe) and ZCO (M_s~ 0.483 emu/g, M_r~0.089 emu/g and H_c~41 Oe) nanorods [Fig.6(a)] that performed weak RTFM. The temperature dependent magnetization measurement of ZFO and ZCO exhibits slight AFM interactions up to low temperature [27].

As shown in Fig.6(b), the weak RTFM of ZFCeO is described due to double exchange mechanism [6] which involve Fe^{2+}-Fe^{3+} transition via oxygen vacancies. The valance states of Fe are given in Fig.8(a). Xiao *et al.* [7] theoretically investigated Fe:ZnO nanoparticles, and have shown that Fe stabilizes polar instable surfaces, while nonpolar surfaces, namely (10$\underline{1}$0) and (11$\underline{2}$0) remain intact. Polar surfaces can be stabilized indirectly through Fe^{2+}-Fe^{3+} pair-assisted charge transfer, which reduces polarity and hence solubility inpolar solvents may be responsible for RTFM. Gilliland *et al.* [3] studied electronic structure of Co and Fe doped ZnO through DFT calculation. It is reported that the occupied α-spin Co 3*d* states are much closer to the valence band maximum which perform a strong mixing of Co $3dz^2$ A_1 singlet with the A_1 O $2p_z$ result into the crystal field splitting. However, all β-spin Fe 3*d* states are inside the conduction band and α-spin bands are at the top of the valence band have strong Fe 3*d* character at which the O 2*p* contribution is dominant [3]. The band gap is found to increase at the rate of 23 and 4 meV/%Co and Fe, respectively. Therefore, hopping mechanism is easily formed with Fe doping at room temperature. However, the Co:ZnO have effective moment per Co as 4.8 μ_B and the total magnetization is reduced, demonstrating that Co-O-Co pairs are AFM [46]. But the pure ZFO and ZCO samples of nanorods [Fig.6(a)]

equally causes RTFM which is described due to defects formation on the surfaces of nanorods. This type of defect-assisted magnetic behavior is described by Pal *et al.* [47] for Co:ZnO nanorods by BMP model. They expect an intrinsic exchange interaction of Co ions and V_{Zn}, O_i related defects of nanorods responsible in long-range ferromagnetism. According to the BMP model, bound electrons (holes) in the defect states can couple with TM ions and cause the ferromagnetic regions to overlap, giving rise to long range ferromagnetic ordering [16].

Instead to pure ZFO and ZCO nanorods, the Ce doped samples are paramagnetic at room temperature, it is due to the formation of strong AFM interactions. The transition between RE and TM ions involve indirect mechanism (4*f*-5*d*-3*d*) in which the strong inter-atomic direct 5*d*-3*d* exchange is transmitted to the 4*f* electrons via the intra-atomic 4*f*-5*d* ferromagnetic interaction [48]. The 5*d*-3*d* exchange is AFM when the 5*d* band is less than half full and the 3*d* band is more than half full, as is the case of RE metals with ferromagnetic 3*d* TM. The TM spin couples antiparallel to the RE spin, but the magnetization of RE and TM sublattices couple parallel in the light RE=Ce, La, Gd element [J = L-S]. Singh *et al.* [49] suggested ferro/AFM coupling in 3*d*-4*f* pairs for V:Gd on the basis of DFT. The transition of $Ce^{3+} - V_{\ddot{O}}$ with TM ions is expected to be AFM [12]. Therefore, from above discussion, it is expected that the transition between Ce with Fe and Co ions in DMS ZnO is AFM at room temperature and the ferromagnetic exchange interactions may be found with varying field or temperature at defect sites.

The temperature-dependent magnetization measurement exhibited in Fig.6(c & d) via ZFC and FC at H=500 Oe and T=300-5 K. The enhanced difference between the ZFC and FC with reducing temperature from 300-5 K indicates that the AFM transitions are converted into ferromagnetic state. Since TM doped ZnO is weak AFM [50, 19]. It results into low magnitude to the ferromagnetism as well as paramagnetic or superparamagnetic behavior at

room temperature. Gopal *et al.* [51] theoretically investigated weak AFM ordering in TM substituted ZnO. Walsh *et al.* [5] also given weak preference to the AFM interactions and stabilization of FM in TM:ZnO. Therefore, the simultaneous doping from TM and RE ions into ZnO may increase AFM ordering to improve ferromagnetism. The enhance bifurcation of FC/ZFC curves and ferromagnetic behavior at low temperature measurement [Fig.6] is an indication to the AFM to ferromagnetic state. A slight dip in ZFC at low temperature is an indication of typically blocking temperature of AFM or Neel temperature (T_N). The shape of M(T) curves is almost concave suggesting predominance of BMP interaction [52, 16]. Coey *et al.* [16] reported that an electron trapped in the defect/oxygen vacancy level creates an F center. Exchange interaction between neighboring magnetic ions mediated by this F center forms a BMP. Overlapping of such polarons contributes to long-range ferromagnetic ordering in Ce doped Fe,Co:ZnO. It has been also observed that the value of H_c is enhanced at low temperature measurement. This is due to some ferromagnetic cluster assemblies exist in the samples [53] which enlarged H_c in the *M-H* hysteresis. In the present case, the ferromagnetic cluster assemblies may arises either from Ce ions with Fe and Co or from magnetic polarons [54]. When particles are connected to form a chain and the magnetic moments between the adjacent particles are noncollinear, the magnetization process is described by a fanning mode [55]. This mechanism leads to a large H_c value [Fig.6 (c'& d')]. Moreover, the enhancement in the magnetic anisotropy is associated with the low symmetric surface atoms and lattice defects are also possible [56].

The transformation of ferromagnetism at low temperature to AFM at room temperature [Fig.6] is described due to localized carriers (defects/vacancies) along with magnetic impurity spins which are most likely to form the magnetic polaron [57]. These magnetic polarons have one localized carrier and many magnetic impurity spins that are surrounded to the localized carriers. These types of magnetic polarons are formed randomly

within the samples and some extra magnetic ions are also present between those magnetic polarons and they are randomly distributed within the ZnO matrix. Wolf *et al.* [58] suggested magnetic polarons due to polaron-polaron interaction model include: (i) the kinetic exchange interaction between the spins of the localized carriers and magnetic impurity inside polarons (interaction parameter *U*), (ii) polaron-polaron interaction through the magnetic ions that situated between the magnetic polarons (interaction parameter *V*), (iii) the virtual hopping of carriers from one site to the other induce AFM interaction (interaction parameter *W*). According to this polaron-polaron pair model [58], we have considered with $a/r \geq 1$ for present DMS system, where *a* is the effective polaronic Bohr radius and *r* is the distance between two nearest magnetic polarons. Different degrees of competition arise between *V* and *W* interaction of magnetic polarons, where $V/W=0$ implies no competition so that the magnetic polaron spins are aligned antiferromagnetically. However, increase in *V*/*W* value suggests the relaxation to AFM coupling between the nearest magnetic polarons. In fact, according to this model [58] further increase *V*/*W* ratio, it will cause ferromagnetic coupling between nearest magnetic polarons. Thus, in the present ZFCeO and ZCCeO samples the observed AFM ground state can be easily understood with this model. The Ce ions may cause an increase in the number of magnetic polarons, as well as an increase in effective polaronic Bohr radius *a*. Xing *et al.* [59] suggested defects due to oxygen vacancies responsible in BMP at low temperature ferromagnetism and room temperature antiferromagnetism.

To further investigate the observed magnetic behavior, the temperature dependent real (χ') and imaginary (χ'') components of the ac magnetic susceptibility of Ce doped ZFO and ZCO nanoparticles at frequencies 100, 300, 500 and 1000 Hz are shown in Fig. 7. The applied oscillating field, H_{ac} is 2.5 Oe without any dc field bias in T = 10 – 100 K. The frequency-independent peak maxima of χ' corresponds to the magnetic phase transition into an AFM state with T_N = 56 and 42 K, respectively, observed for ZFCeO and ZCCeO

samples. A similar magnetic transition for AFM-ferromagnetic transition has been also observed by M. Balanda *et al.* [60]. This observation is correlated with variation in magnetization in the ZFC and FC measurement given in Fig.6. A slight dispersion in the $\chi'(T)$ curve after peak maxima is also observed. It indicates the existence of certain spin-glass, ferromagnetic cluster and the cluster-glass magnetic type states in the samples [61]. It is also reflecting the slow magnetic relaxation [62]. However, the peak in $\chi''(T)$ increases with decreasing frequency. This is qualitatively different from the behavior of most spin glasses in which we expect an increase of the peak magnitude with increasing frequency [63]. This also induced certain peak shifting with frequency. Thus, the obtained ac magnetization data support the formation of the AFM DMS materials with certain cluster-glass formation than that of classic spin-glass one.

In addition, the existence of RTFM and PL quenching in the visible region for ZFCeO must depends upon the valance states of Fe and Ce ions. Therefore, we have studied the valance states of Fe and Ce for ZFCeO by XPS spectra. Figure 8 (a) shows the Fe 2p states in the binding energy region 707–728 eV. It was reported [64] that Fe 2p photoelectron peaks from oxidized iron are associated with satellite peaks, which is important for identifying the chemical states. The Fe^{2+} and Fe^{3+} $2p_{3/2}$ peaks always show satellite peaks at 6 eV and 8 eV above the principal peaks at 709.5 eV and 711.2 eV, respectively. In Fig. 8 (a), the satellite peaks were found in the energy region of 6-8 eV above the $2p_{3/2}$ principal peak. It indicates that for ZFCeO DMS nanoparticles, Fe coexists in both Fe^{2+} and Fe^{3+} states. For this, a Gaussian fitting of Fe 2p peaks with satellites is also performed to show peaks corresponding to Fe^{2+} (709.60 and 722.51 eV) and Fe^{3+} (710.82 and 723.97 eV). It indicates that the Fe ions are mixed valences of 2+ and 3+ states. The difference in energy between the Fe $2p_{3/2}$ and $2p_{1/2}$ peaks resulting from spin-orbit coupling is ~13.46 eV, which is very close to the reported value of Fe 2p [65]. The peaks related to $2p_{3/2}$ 709.89 eV and $2p_{1/2}$ 723.35 eV are

observed. The position of satellite peak is 716.77 eV. Therefore, it is evaluated from Fe 2p XPS spectrum that the Fe exist into mixed Fe^{2+} and Fe^{3+} oxidation states and contribute ferromagnetism [Fig.6(b)] at room temperature due to Fe^{2+}-Fe^{3+} transition via oxygen vacancies.

The optical quenching for ZFCeO shown in Fig.5(a) is related with valance states of Ce ions in it and given by XPS spectra shown in Fig. 8(b). The XPS spectra for Ce 3*d* indicate the presence of a mixed valence state (Ce^{3+}/Ce^{4+}) of ZFCeO. The peaks at 881.68, 898.05, 899.87 and 916.25 eV are associated to Ce^{4+}, while the peaks at 884.33 and 903.51 eV are associated to Ce^{3+} [66]. These two different oxidation states existing in Ce ions (Ce^{4+} and Ce^{3+}) are responsible in optical enhancement [11]. Under oxidation conditions, all Ce^{3+} ions are converted into Ce^{4+} ions which led to the quenching of the blue and green emissions.

Electronic structure of Ce doped Fe:ZnO and Co:ZnO DMS is investigated by means of DFT calculations using PAW method within GGA-PBE schemes shown in Fig.9 (a-d). For ZFCeO, the binding energy of the relaxor Wurtzite structure correspond to nearest neighbor Ce substituted Zn to Fe [Fig.9(a) with $l_{Ce\text{-}Fe}$ = 2.80 Å], E_a= -2932.691869 Ha and non-nearest neighbor Ce(Zn) to Fe [Fig.9(b) with $l_{Ce\text{-}Fe}$ = 4.72 Å], E_b= -2932.676185 Ha. The difference, $\Delta E = E_a - E_b$ = -426.783 meV. However for ZCCeO, the binding energy correspond to nearest neighbor Ce(Zn) to Co [Fig.9(c) with $l_{Ce\text{-}Co}$ = 2.66 Å], E_c= -2971.987503 Ha and non-nearest neighbor Ce(Zn) to Co [Fig.9(d) with $l_{Ce\text{-}Co}$ = 4.74 Å], E_d= -2971.963521 Ha. The difference, $\Delta E = E_c - E_d$ = -652.583 meV. The enhancement in the difference ΔE indicates that the Ce atom is more stable when replaced by those Zn that nearest neighbor to TM:Fe,Co. Also, the calculated value of ΔE for ZCCeO is higher than ZFCeO. It indicates that the Ce(Zn) atom [Fig.9(c)] is more stable with Co than Fe [Fig.9(a)].

Gopal *et al.* [49] studied the nature of magnetic interactions in TM-doped ZnO using the LSDA+U (spin polarized LDA with Hubbard U parameter) method, and the results

indicate that the AFM ordering is favorable. Using a similar DFT calculation for Co doped ZnO, Hu *et al.* [67] suggested the AFM order between nearest-neighbor magnetic ions via oxygen vacancy. In higher doping Co concentration, Zn atoms would be entirely substituted by Co in a large region, forming a lot of Co-O-like clusters in Wurtzite structure. Therefore, we have assumed that the effect of Ce into Co:ZnO strengthen the AFM behavior. This is due to AFM character of Co doped ZnO and higher stability of Ce with the nearest-neighbor Co atom in the Wurtzite ZnO. Also for Fe doped ZnO, Xiao *et al.* [19] used DFT theory and predict AFM ordering. In addition, we have also analyzed from Fig.9 that the doping of Ce ions into Fe:ZnO and Co:ZnO results into variation in bond length between Zn, O, Fe, Co and Ce atoms which may induce defects or vacancies in the Wurtzite lattice.

4. Conclusion

DMS ZFCeO and ZCCeO nanoparticles have been synthesized by sol-gel process. XRF measurements identify the chemical composition which consistent with the stoichiometric ratio taken for ZFCeO and ZCCeO. XRD pattern indicate Wurtzite ZnO structure and the influence of Ce on lattice is investigated by calculating lattice constants. The average size, D, of nanoparticles is 97±4 nm and 106±3 nm, respectively, for ZFCeO and ZCCeO. The nanoparticles are formed in the Ce doped sample due to larger ionic radii difference among Ce and Fe,Co:ZnO ions and their reactivity with OH^-. The nonpolar optical phonon E_2 (high) mode of ZnO present Wurtzite structure and the variation in Raman modes induce lattice defects/vacancies. PL spectra shown NBE emission due to ZnO energy gap and the visible emission is enhanced due to the production of defects. The ZFC and FC magnetization measurement at H=500 Oe and T=300-5 K show AFM-ferromagnetic transition. At 5 K, the value of M_s is 0.339 and 0.478 emu/g, respectively, measured for ZFCeO and ZCCeO. The ac magnetic susceptibility measurement, $\chi'(T)$ and $\chi''(T)$, indicates the value of T_N = 56 and 42 K, respectively, for ZFCeO and ZCCeO and some ferromagnetic

clustered growth below T_N is also found. For ZFCeO, the weak RTFM is formed due to mixed valance states Fe^{2+}/Fe^{3+} and optical confinement due to oxidizing Ce^{3+} to Ce^{4+} via oxygen vacancy. Using DFT calculation, we have analyzed that the Ce atoms replaced those Zn site in the Wurtzite structure that nearest-neighbor to TM:Fe,Co atoms.

Acknowledgment

The authors are acknowledged the Sophisticated Analytical Instrumentation facility (SAIF) of Panjab University, Chandigarh for XRD, TEM and XRF measurement. The author Kuldeep Chand Verma is also grateful to the Chairperson, Department of Physics, Panjab University, Chandigarh, for providing constant encouragement, motivation, and support to carry out this work.

References

1. T. Dietl, H. Ohno, F. Matsukura, J. Cibert and D. Ferr, *Science*, 2000, **287**, 1019-1022.

2. J.K. Furdyna, *J. Appl. Phys.*, 1988, **64**, R29-R64.

3. S.J. Gilliland, J.A. Sans, J.F. Sanchez, G. Almonacid, B.G. Domene, A. Segura, G. Tobias and E. Canadell, *Phys. Rev B*, 2012, **86***,* 155203-13.

4. I. Djerdj, Z. Jaglicic, D. Arcon and M. Niederberger, *Nanoscale*, 2010, **2**, 1096-1104.

5. A. Walsh, J.L.F. Da Silva and S.H. Wei, *Phys. Rev. Lett.*, 2008, **100**, 256401-4

6. C. Zener, *Phys. Rev.*, 1951, **82**, 403-405.

7. J. Xiao, A. Kuc, T. Frauenheim and T. Heine, *Phys. Rev. Lett.*, 2014, **112**, 106102-5

8. J.M.D.Coey, K. Wongsaprom, J. Alaria and M. Venkatesan, *J. Phys. D: Appl. Phys.*, 2008, **41**, 134012-6

9. J.J. Beltran, C.A. Barrero and A. Punnoose, *J. Phys. Chem. C*, 2014, **118**, 13203.

10. J.J. Beltran, J.A. Osorio, C.A. Barrero, C.B. Hanna and A. Punnoose, *J. Appl. Phys.*, 2013, **113**, 17C308-3.

11. G.A. Babu, G. Ravi, T. Mahalingam, M. Navaneethan, M. Arivanandhan and Y. Hayakawa, *J. Phys. Chem. C*, 2014, **118**, 23335-23348.

12. M. Nakayama, H. Ohshima, M. Nogami and M.A. Martin, *Phys. Chem. Chem. Phys.*, 2012, **14**, 6079-608.

13. Y. Utsumi, J. Martinek, H. Imamura, P. Bruno and S. Maekawa, *J. Magn. Magn. Mater.*, 2007, **310**, 1142-1144

14. B. Yao, P. Wang, S. Wang and M. Zhang, *CrystEngComm*, 2014, **16**, 2584-2588

15. H. Y. Hwang, S.W. Cheong, P. G. Radaelli, M. Marezio and B. Batlogg, *Phys. Rev. Lett.*, 1995, **75**, 914-4.

16. J.M.D. Coey, M. Venkatesan and C.B. Fitzgerald, *Nat. Mater.*, 2005, **4**, 173-179.

17. H. L. Meyerheim, C. Tusche, A. Ernst, S. Ostanin, I.V. Maznichenko, K. Mohseni, N. Jedrecy, J. Zegenhagen, J. Roy, I. Mertig and J. Kirschner, *Phys. Rev. Lett.*, 2009, **102**, 156102

18. G. S. Chang, E. Z. Kurmaev, D. W. Boukhvalov, L. D. Finkelstein, S. Colis, T. M. Pedersen, A. Moewes and A. Dinia, *Phys. Rev. B*, 2007, **75**, 195215.

19. J. Xiao, T. Frauenheim, T. Heine and A. Kuc, *J. Phys. Chem. C*, 2013, **117**, 5338

20. S. A. Aravindh, U. Schwingenschloegl and I. S. Roqan, *J. Appl. Phys.*, 2014, **116**, 233906

21. I. Bantounas, V. Singaravelu, I. S. Roqan and U. Schwingenschlogl, *J. Mater. Chem. C*, 2014, **2**, 10331

22. X. Gonze, B. Amadon, P.M. Anglade, J.M. Beuken, F. Bottin, P. Boulanger, F. Bruneval, D. Caliste, R. Caracas and M. Cote, *J. Comput. Phys. Comm.*, 2009, **180**, 2582-2615

23. F. Jollet, M. Torrent and N. Holzwarth, *Comp. Phys. Commun.*, 2014, **185**, 1246-1254.

24. P. R. L. Keating, D.O. Scanlon, B.J. Morgan, N.M. Galea and G.W. Watson, *J. Phys. Chem. C*, 2012, **116**, 2443.

25. H. J. Monkhorst and J. D. Pack, *Phys. Rev. B*, 1976, **13**, 5188

26. S.M. Zhou, H.C. Gong, B. Zhang, Z.L. Du, X.T. Zhang and S.X. Wu, *Nanotechnology*, 2008, **19**, 175303-4

27. R.K. Kotnala, V. Gupta and K.C. Verma, *Curr. Appl. Phys.*, 2014, **14**, 749

28. S. Kumar, S. Basu, B. Rana, A. Barman, S. Chatterjee, S.N. Jha, D. Bhattacharyya, N. K. Sahoo and A. K. Ghosh, *J. Mater. Chem. C*, 2014, **2**, 481

29. W.M. Hosny and P.A. Khalaf-Alaa, *Int. J. Electrochem. Sci.*, 2013, **8**, 1520

30. A. Kawska, P. Duchstein, O. Hochrein and D. Zahn, *Nano Lett.*, 2008, 8, 2336

31. F. Ahmed, S. Kumar, N. Arshi, M.S. Anwar and B.H. Koo, *CrystEngComm*, 2012, **14**, 4016.

32. M. Zhang, K. Chen, Y. Chen, Y. Peng, X. Sun and D. Xue, *CrystEngComm*, 2015, **17**, 1917.

33. X.H. Xia, J.P. Tu, Y.Q. Zhang, Y.J. Mai, X.L. Wang, C.D. Gu and X.B. Zhao, *J. Phys. Chem. C*, 2011, **115**, 22662.

34. T.D. Nguyen, C.T. Dinh and T.O. Do, *Inorg. Chem.*, 2011, **50**, 1309

35. C. Xu and X. Qu, *NPG Asia Mater.*, 2014, **6**, e90

36. D.E. Motaung, G.H. Mhlongo, S.S. Nkosi, G.F. Malgas, B.W. Mwakikunga, E. Coetsee, H.C. Swart, H.M.I. Abdallah, T. Moyo and S.S. Ray, *ACS Appl. Mater. Interf.*, 2014, **6**, 8981.

37. H.B. Carvalho, M.P.F. Godoy, R.W.D. Paes, M. Mir, A.O. Zevallos, F. Iikawa, M.J.S.P. Brasil, V.A. Chitta, W.B. Ferraz, M.A. Boselli and A.C.S. Sabioni, *J. Appl. Phys.*, 2010, **108**, 033914.

38. N.P. Herring, L.S. Panchakarla and M.S. El-Shall, *Langmuir*, 2014, **30**, 2230.

39. R. Cusco, E.A. Llado, J. Ibanez, L. Artus, J. Jimenez, B. Wang and M.J. Callahan, *Phys. Rev. B*, 2007, **75**, 165202

40. B. Panigrahy, M. Aslam, and D. Bahadur, *Nanotechnology*, 2012, **23**, 115601

41. L.N. Tong, T. Cheng, H.B. Han, J.L. Hu, X.M. He, Y. Tong and C.M. Schneider, *J. Appl. Phys.*, 2010**, 108**, 023906

42. G. Vijayaprasath, R. Murugan, G. Ravi, T. Mahalingam and Y. Hayakaw, *Appl. Surf. Sci.*, 2014, **313**, 870

43. S. Sharma, B.D. Mukri and M.S. Hegde, *Dalton Trans.*, 2011, **40**, 11480.

44. G.R. Li, X.H. Lu, Z.L. Wang, X.L. Yu and Y.X. Tong, *Electrochimica Acta*, 2010, **55**, 3687

45. F. Gu, S.F. Wang, M.K. Lu, G.J. Zhou, D. Xu and D.R. Yuan, *Langmuir*, 2004, **20**, 3528

46. A. Ney, K. Ollefs, S. Ye, T. Kammermeier, V. Ney, T.C. Kaspar, Chambers, F. Wilhelm and A. Rogalev, *Phys. Rev. Lett.*, 2008, **100**, 157201.

47. B. Pal, S. Dhara, P.K. Giri and D. Sarkar, *J. Alloys Compd.*, 2014, **615**, 378

48. M.S.S. Brooks and B. Johansson, Handbook of Magnetic Materials. Elsevier, Amsterdam, Vol. 7, Chap. 3.

49. S.K. Singh and G. Rajaraman, *Dalt. Trans.*, 2013, **42**, 3623.

50. D.D. Sarma, R. Viswanatha, S. Sapra, A. Prakash and M. Garcia- Hernandez, *J. Nanosci. Nanotechnol.*, 2005, **5**, 1503

51. P. Gopal and N.A. Spaldin, *Phys. Rev. B*, 2006, **74**, 094418

52. A. Kaminski and S.D. Sarma, *Phys. Rev. Lett.*, 2002, **88**, 247202.

53. S. Yamamuro, K. Sumiyama, T. Kamiyama and K. Suzuki, *J. Appl. Phys.*, 1999, **86**, 5726

54. N.N. Kovaleva, K.I. Kugel, A.V. Bazhenov, T.N. Fursova, W. Loser, Y. Xu, G. Behr and F.V. Kusmartsev, *Sci. Rep.*, 2012, **890**, 1-7

55. I.S. Jacobs and C.P. Bean, *Phys. Rev.*, 1955, **100**, 1060

56. M. Respaud, J.M. Broto, H. Rakoto, A.R. Fert, L. Thomas, B. Barbara, M. Verelst, E. Snoeck, P. Lecante and A. Mosset, *Phys. Rev. B*, 1998, 57, 2925

57. S.K. Mandal, A.K. Das, T.K. Nath, D. Karmakar and B. Satpati, *J. Appl. Phys.*, 2006, **100**, 104315

58. P.A. Wolf, R.N. Bhatt and A.C. Durst, *J. Appl. Phys.*, 1996, **79**, 5196

59. G. Z. Xing, J.B. Yi, D.D. Wang, L. Liao, T. Yu, Z.X. Shen, C.H.A. Huan, T.C. Sum, J. Ding and T. Wu, *Phys. Rev. B*, 2009, **79**, 174406

60. M. Balanda, *Acta Physica Pol. A*, 2013, **124**, 964.

61. Satyapal Singh Rathore and Satish Vitta, *Sci. Rep.*, 2015, **5**, 9751

62. E.V. Sampathkumaran and A. Niazi, Phys. Rev. B, 2002, 65, 180401

63. E. Fertman, S. Dolya, V. Desnenko, A. Beznosov, M. Kajnakova and A. Feher, *J. Magn. Magn. Mater.*, 2012, **324**, 3213

64. K.C. Verma, S. K. Tripathi and R. K. Kotnala, Magneto-Electric/Dielectric and Fluorescence Effects in Multiferroic $xBaTiO_3$-(1 -x)$ZnFe_2O_4$ Nanostructures, *RSC Adv.*, 2014, **4**, 60234

65. J. F. Moulder, W. F. Stickle, P. E. Sobol and K. D. Bomben, Handbook of X-ray Photoelectron Spectroscopy Physical Electronics, reissue edn., 1995.

66. Y. Xiong, S. Chen, F. Ye, L. Su, C. Zhang, S. Shen and S. Zhao, *Chem. Comm.*, 2015, **51**, 4635

67. S.Hu, S. Yan, M. Zhao and L. Mei, *Phys. Rev. B*, 2006, **73**, 245205

Figure Captions

Fig.1 XRF pattern of (a) $Zn_{0.94}Fe_{0.03}Ce_{0.03}O$ (ZFCeO) and (b) $Zn_{0.94}Co_{0.03}Ce_{0.03}O$ (ZCCeO) nanoparticles measured at room temperature. The composition of Zn, Fe, Co and Ce is given and well consistent with stoichiometric ratio of ZFCeO and ZCCeO precursor solution.

Fig.2 Rietveld refinement of the XRD pattern of ZFCeO and ZCCeO nanoparticles by using the FullProf program.

Fig.3 TEM images of ZFCeO and ZCCeO nanoparticles at different magnification. The inset on TEM images (right) is the HRTEM image and left the SAED patterns.

Fig.4 Raman spectra (a) ZFO and ZFCeO, and (b) ZCO and ZCCeO nanoparticles measured at room temperature.

Fig.5 PL spectra in the wavelength region 325-650 nm (a) ZFO and ZFCeO (b) ZCO and ZCCeO nanoparticles.

Fig.6 (a) M-H hysteresis of pure ZFO and ZCO nanorods at 300 K (~room temperature). **(b)** M-H hysteresis of ZFCeO and ZCCeO nanoparticles at 300 K. **(c & d)** Magnetization (*M*) as a function of temperature (*T*) following ZFC and FC at H = 500 Oe for Ce doped samples. Insets **(c' & d')** show respective *M-H* hysteresis measured at 5 K.

Fig.7 Temperature dependent real part of the ac magnetic susceptibility (χ') of ZFCeO and ZCCeO nanoparticles at T = 10 – 100 K. The measurement was performed at an oscillating field H_{ac} = 2.5 Oe for frequencies of 100, 300, 500 and 1000 Hz without any dc field bias. The inset shows the temperature dependence of the imaginary part of the ac magnetic susceptibility (χ''), respectively.

Fig.8 XPS spectrum of ZFCeO nanostructure at room temperature: (a) Fe 2p [A Gaussian fitting of 2p peaks with satellite (indicated by pink and green solid line) shows splitting of Fe ions into mixed valence state 2+ and 3+]. (b) Ce 3d (showing the presence of both $Ce^{3+}$and Ce^{4+} valence states) binding energy spectra.

Fig.9 Atomic representation of the ZnO supercell used for Ce doping into Fe:ZnO and Co:ZnO carried out by the first-principles calculation based on the DFT. The Ce atom is placed on Zn site that nearest-neighbor to TM:Fe,Co (a) & (c), and non-nearest-neighbor to TM:Fe,Co atoms (b) & (d), respectively. The bond distance between atoms is measured in Å. Energy difference between configuration (a) and (b), ΔE, E_a-E_b = -426.783 meV, and (c) and (d), ΔE, E_c-E_d = -652.583 meV.

Table 1 Compare the structural and ferromagnetic parameters of pure and Ce doped ZFO and ZCO nanostructure. The ferromagnetism of pure ZFO and ZCO at room temperature and ZFCeO and ZCCeO at 5 K is given.

Sample	*a* (Å)	*c* (Å)	$l_{Zn\text{-}O}$ (Å)	V(Å^3)	*D* (nm)	*L* (nm)	M_s (emu/g)	M_r (emu/g)	H_c (Oe)
ZFO [27]	3.257	5.207	1.9808	47.834	14	50	0.459	0.059	35
ZCO [27]	3.256	5.206	1.9825	47.796	63	131	0.483	0.089	41
ZFCeO	3.260	5.214	1.9829	47.987	97±4	-	0.339	0.135	753
ZCCeO	3.261	5.217	1.9837	48.044	106±3	-	0.478	0.162	197

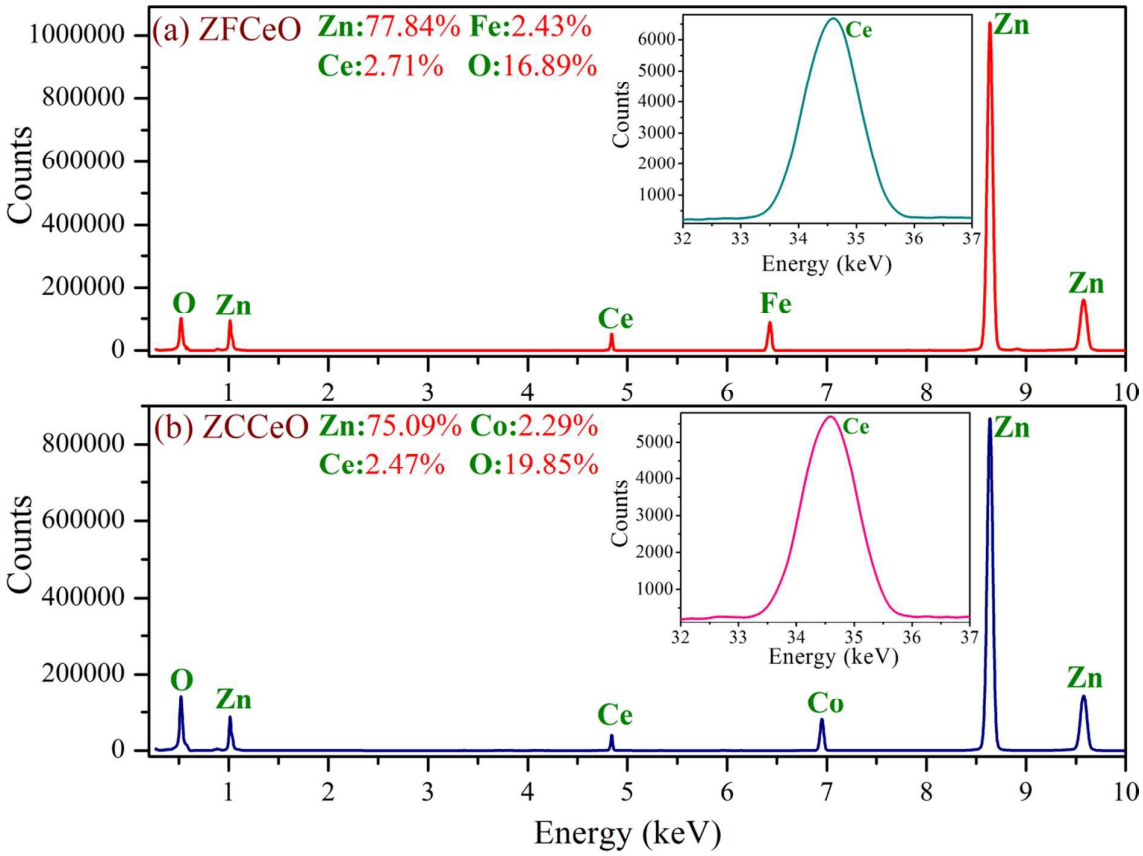

Fig.1

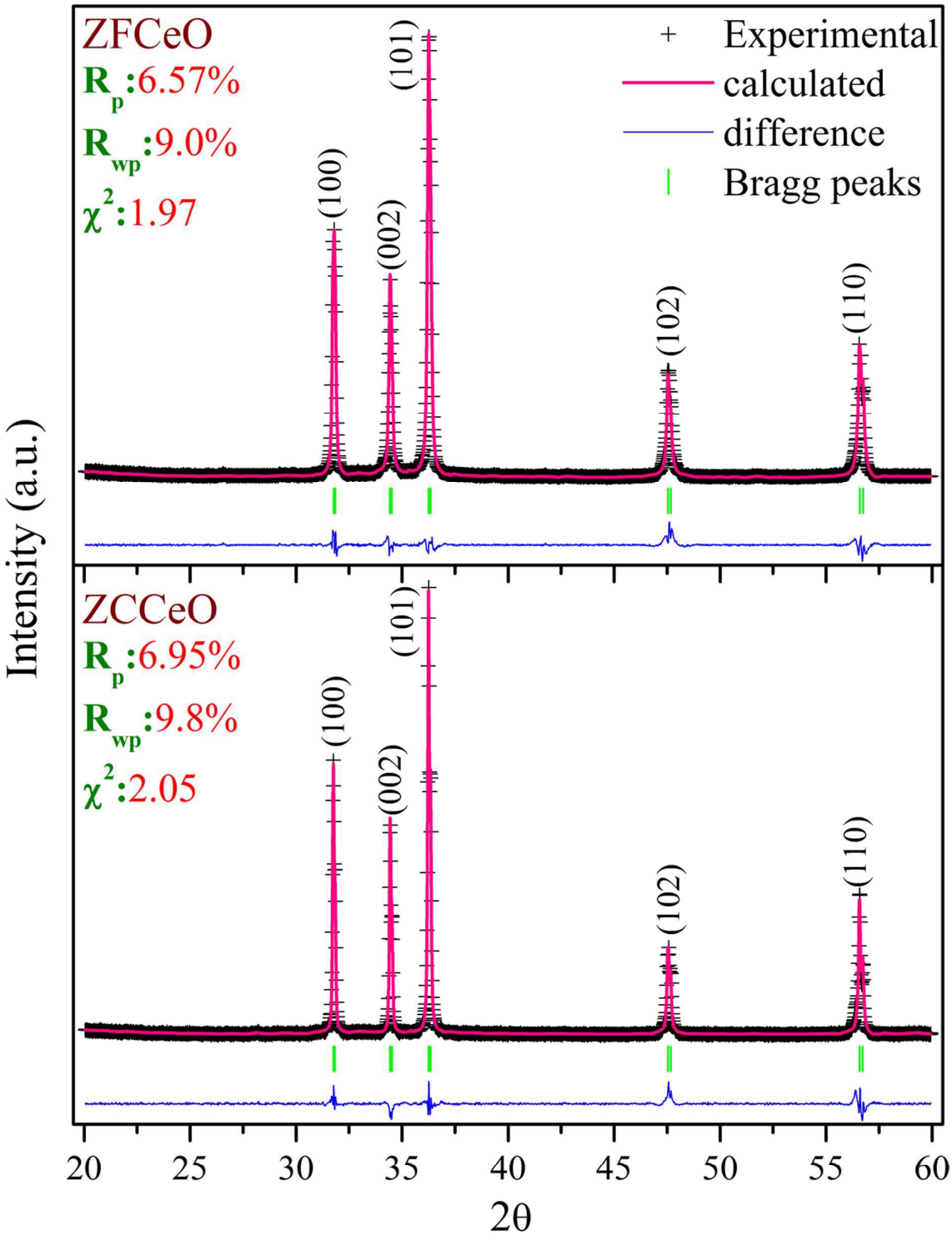

Fig.2

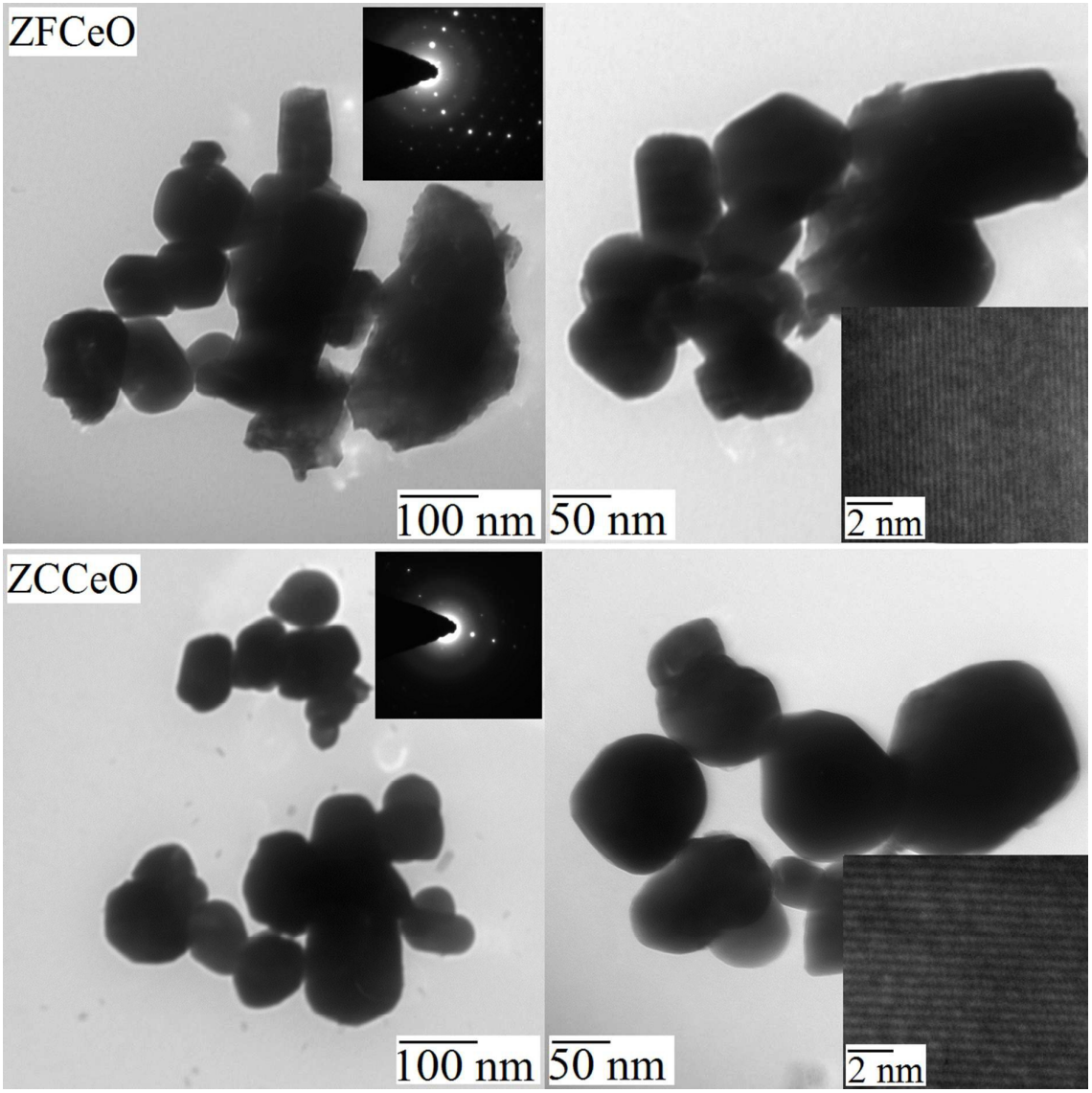

Fig.3

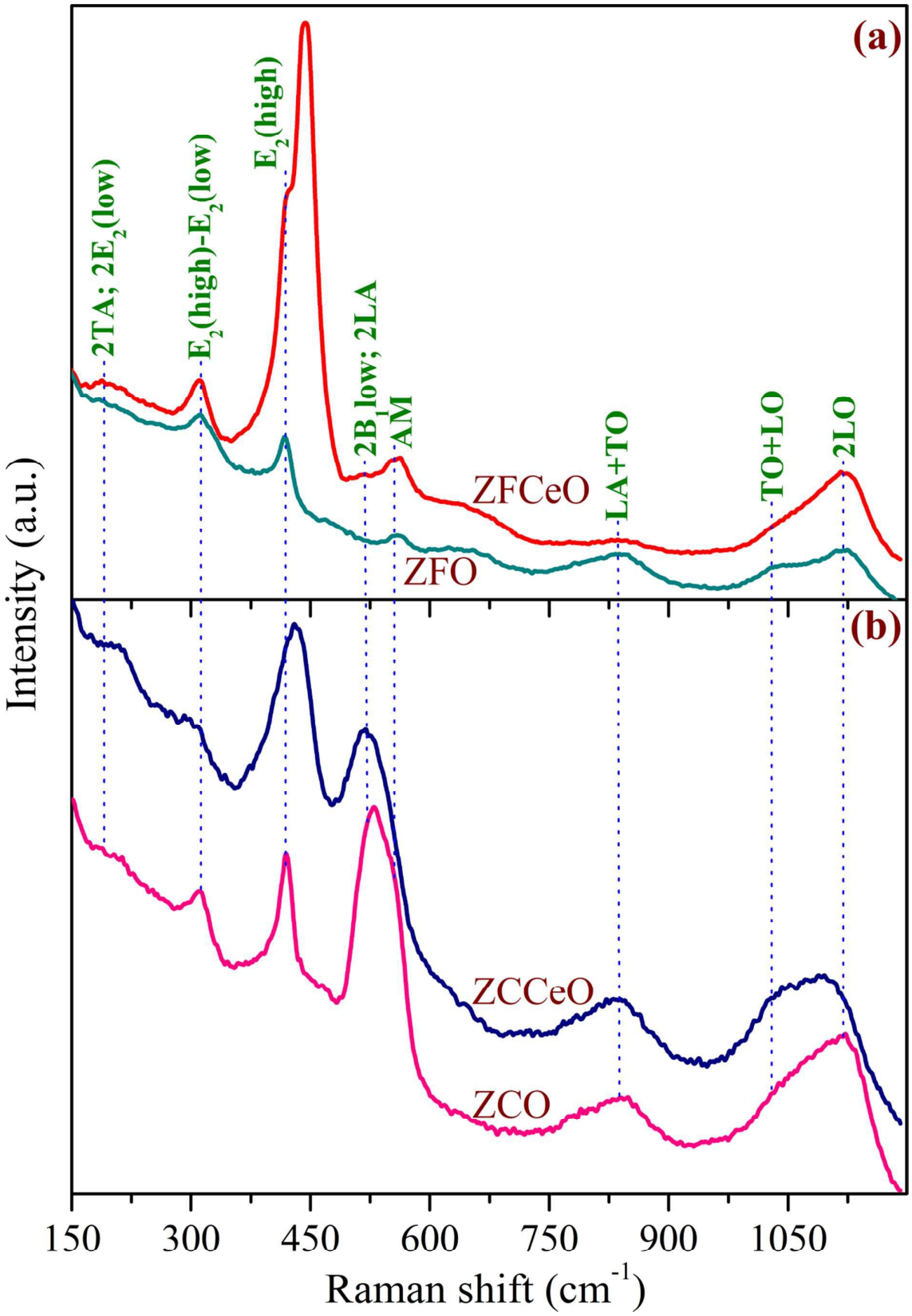

Fig.4

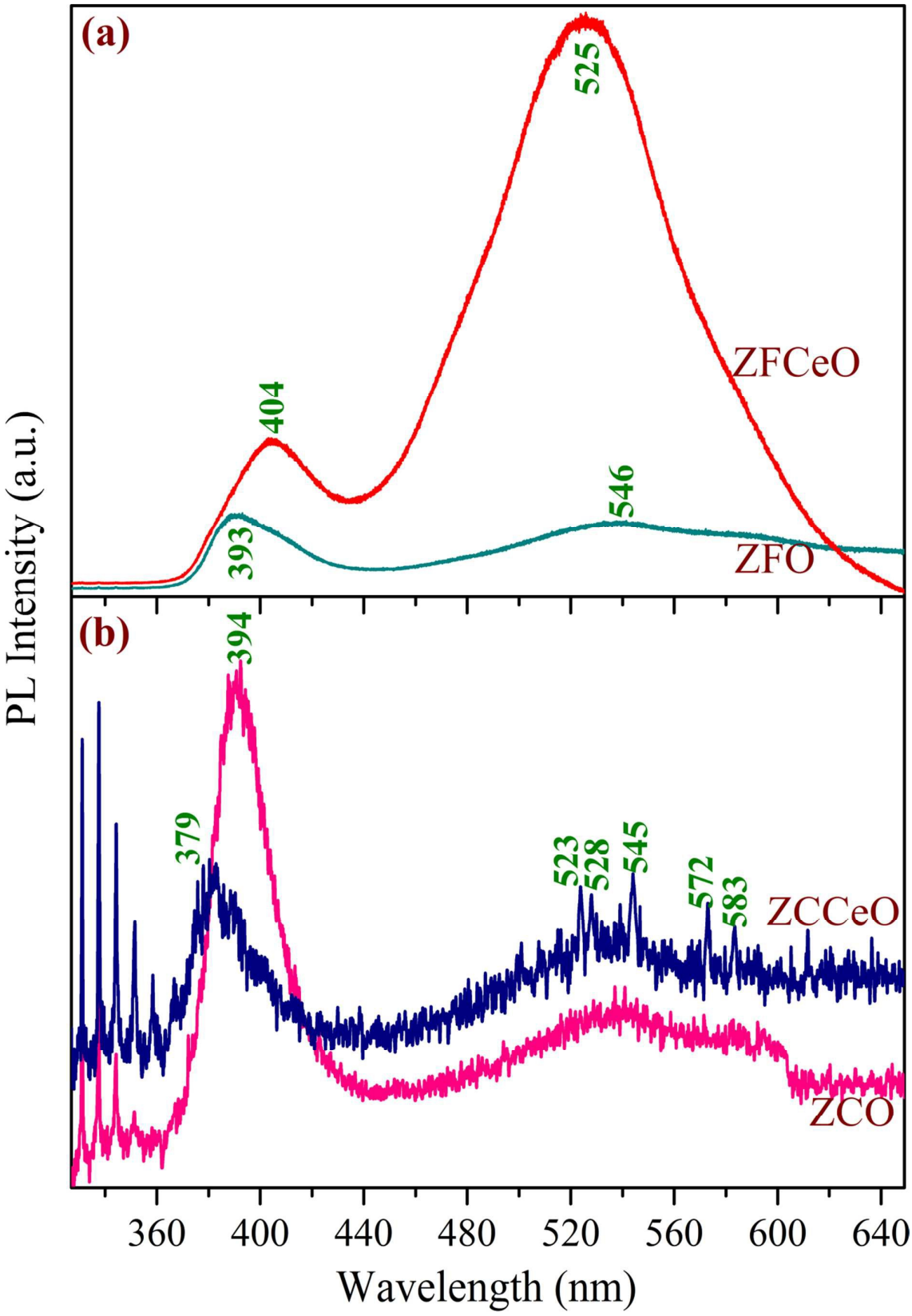

Fig.5

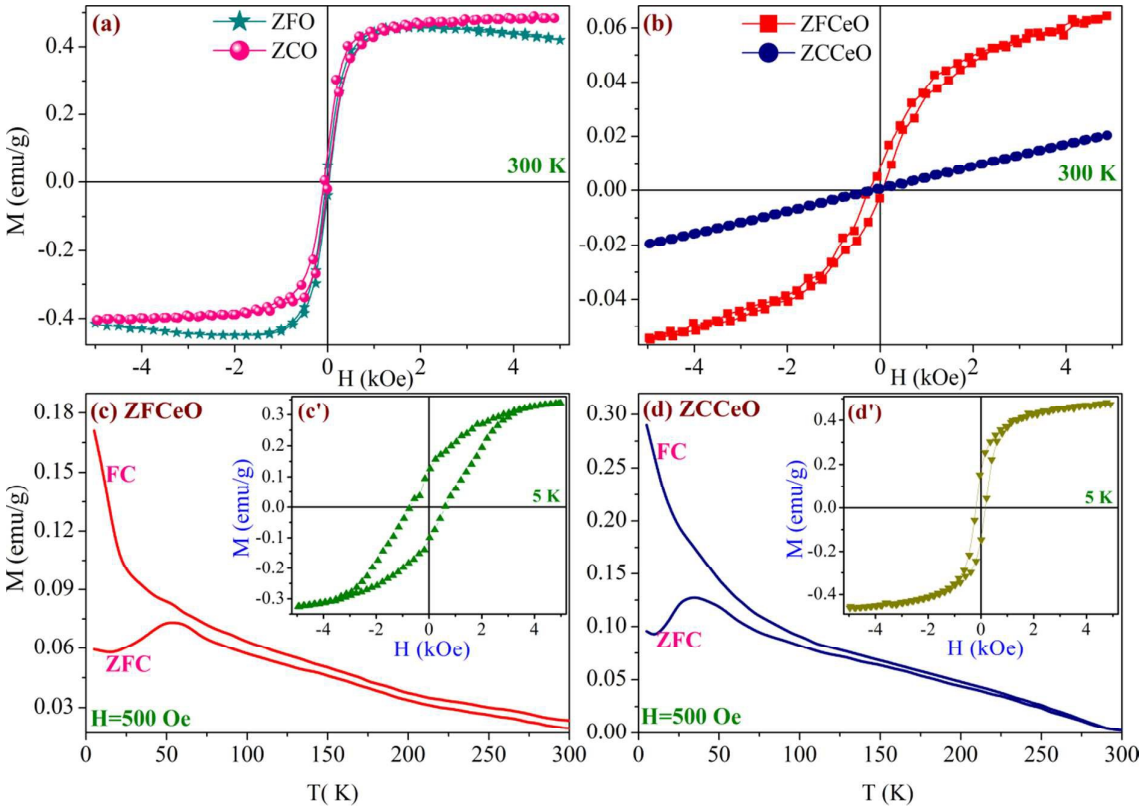

Fig.6

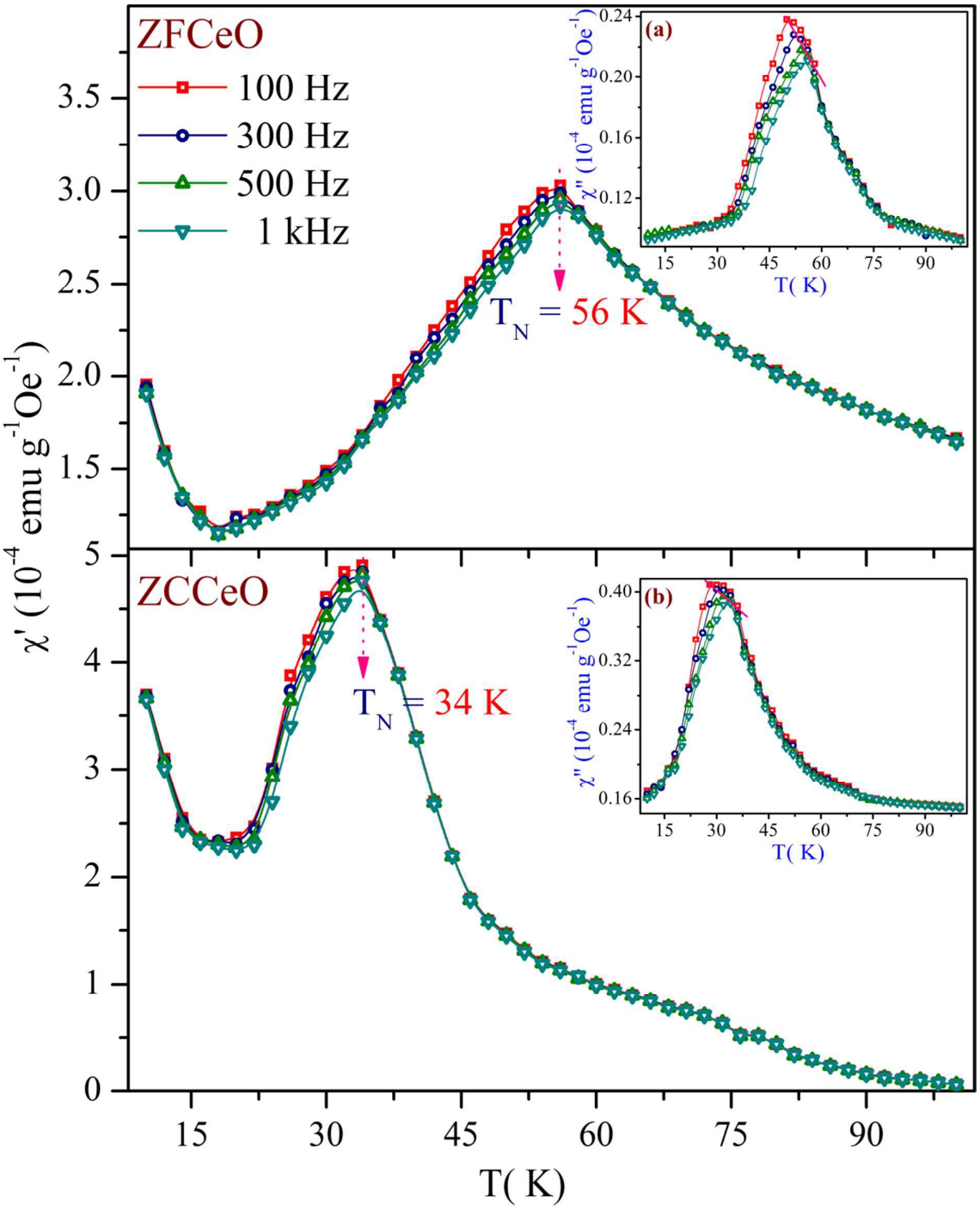

Fig.7

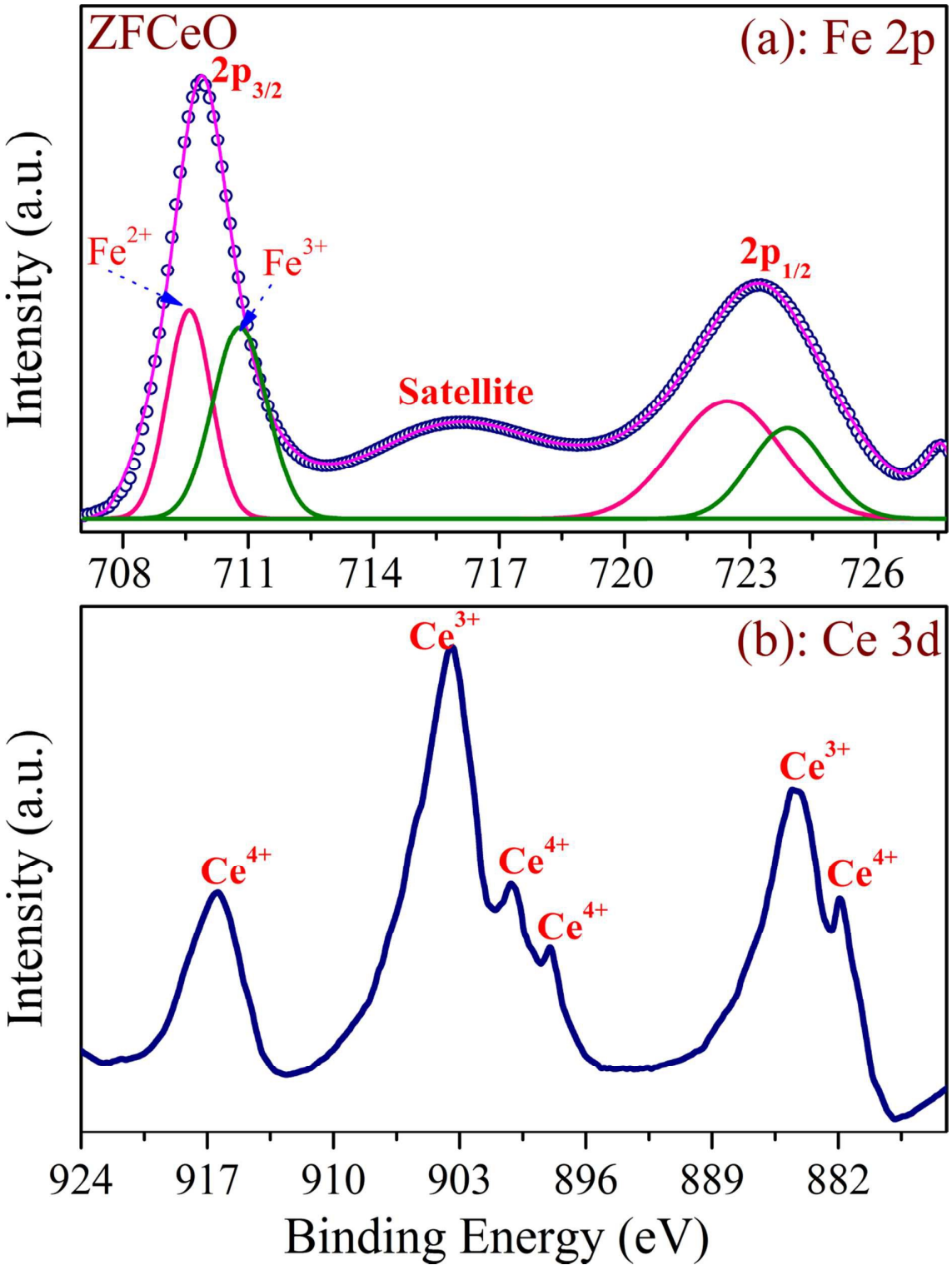

Fig.8

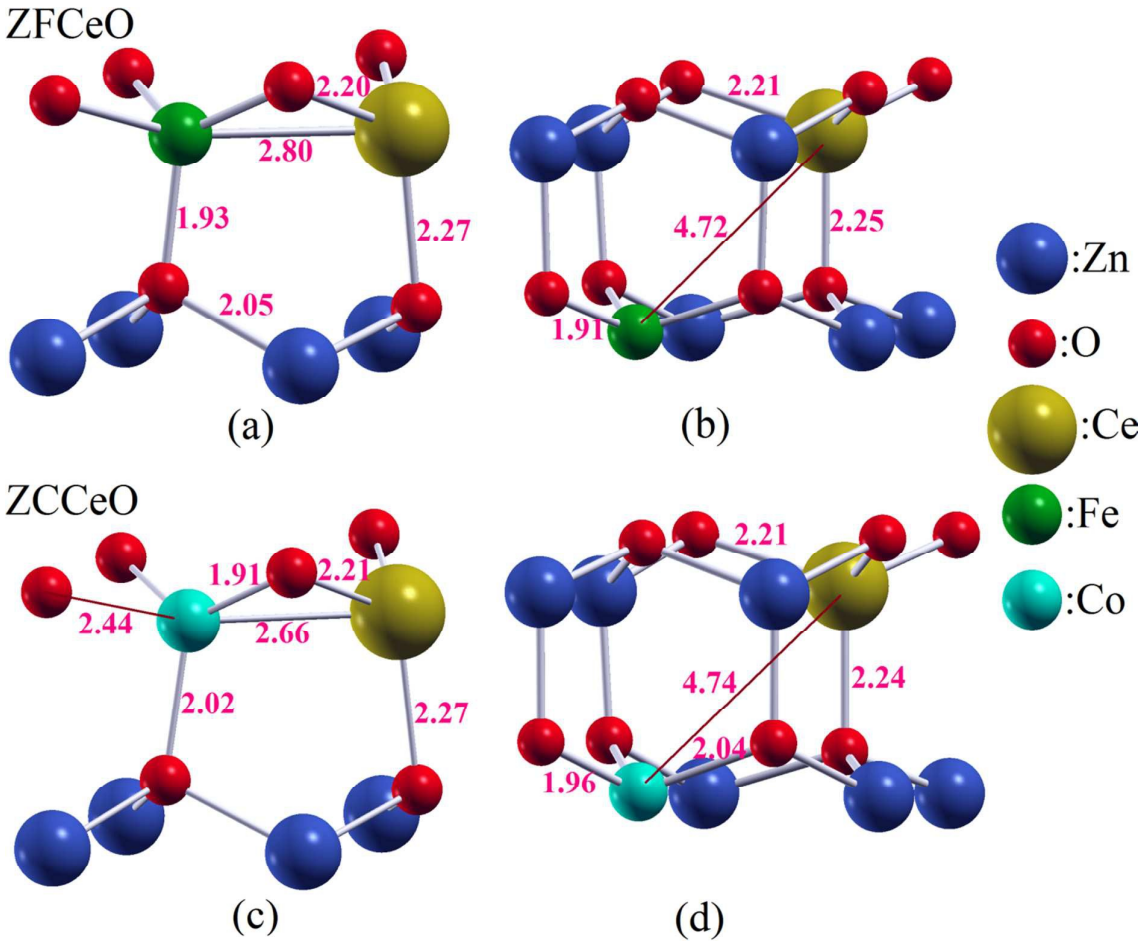

Fig.9

Graphical Abstract